2022

An effective model for the iris regional characteristics andclassification using deep learning alex network

Thiyaneswaran Balashanmugam

Kumarganesh Sengottaiyan

Martin Sagayam Kulandairaj

Helen Dang
Molloy University, hdang@molloy.edu

Received: 18 February 2022 | Revised: 27 August 2022 | Accepted: 7 September 2022

IET Image Processing

DOI: 10.1049/ipr2.12630

The Institution of Engineering and Technology WILEY

ORIGINAL RESEARCH

An effective model for the iris regional characteristics and classification using deep learning alex network

Thiyaneswaran Balashanmugam[1] | **Kumarganesh Sengottaiyan**[2] | **Martin Sagayam Kulandairaj**[3] | **Hien Dang**[4]

[1]Department of ECE, Sona College of Technology, Salem, Tamil Nadu, India

[2]Department of ECE, Knowledge Institute of Technology, Salem, Tamil Nadu, India

[3]Department of ECE, Karunya Institute of Technology and Sciences, Coimbatore, Tamil Nadu, India

[4]Faculty of Computer Science and Engineering, Thuyloi University, Hanoi, Vietnam

Correspondence
Hien Dang, Faculty of Computer Science and Engineering, Thuyloi University, Hanoi 100000, Vietnam.
Email: hiendt@tlu.edu.vn

Abstract

Iris biometrics is one of the fastest-growing technologies, and it has received a lot of attention from the community. Iris-biometric-based human recognition does not require contact with the human body. Iris is a combination of crypts, wolflin nodules, concentrated furrows, and pigment spots. The existing methods feed the eye image into deep learning network which result in improper iris features and certainly reduce the accuracy. This research study proposes a model to feed preprocessed accurate iris boundary into Alexnet deep learning neural network-based system for classification. The pupil centre and boundary are initially recorded and identified from the given eye images. The iris boundary and the centre are then compared for the identification using the reference pupil centre and boundary. The iris portion, exclusive feature of the pupil area is segmented using the parameters of multiple left-right point (MLRP) algorithms. The Alexnet deep learning multilayer networks 23, 24, and 25 are replaced according to the segmented iris classes. The remaining Alexnet layers are trained using the square gradient decay factor (GDF) in accordance with the iris features. The trained Alexnet iris is validated using suitable classes. The proposed system classifies the iris with an accuracy of 99.1%. The sensitivity, specificity, and F1-score of the proposed system are 99.68%, 98.36%, and 0.995. The experimental results show that the proposed model has advantages over current models.

1 | INTRODUCTION

The identity and authentication of humans are currently the most important factors. External identity sources, such as radio frequency identification enabled identity cards and magnetic interface cards, lead to malfunction. Visible human parts such as the finger, palm, face, nose shape, ear shape, vein patterns, lip shape, sclera, and iris can be used as the internal sources for human identity. An extraction feature in the form of matrix data is called a biometric feature. Gait, signature, and keystroke are external human sources of identity that are based on human activity. Single- or multi-model biometric sources are used for human identity. In the case of multi-modal biometrics, two or more biometric sources are used. Forensic science is another technique used for human identity. This is slightly different from biometrics. In the case of biometrics, information is digitally captured in the form of images or sensor data. In the forensic-based approach, human information samples, such as deoxyribonucleic acid and body odors, are used for the identification. The human eye consists of biometric sources, such as the iris, retina, and sclera.

The eye image sample is shown in Figure 1. It consists of eye protective layers such as the upper and lower eyelids. The eyelash is projected from both the eyelids. The iris is varying in colour and is located in the sclera. The iris is circular in size. There are many features that can be extracted from the iris for human identity. It provides uniqueness to every individual, even to differentiate among twins and also between the left and right eyes. The pupil is the innermost layer of the iris. The pupil size varies depending on the light intensity. The pupil is located at the centre of iris as a part of the eye. The major obstacles to form iris segmentation from the eye are the eyelashes and the

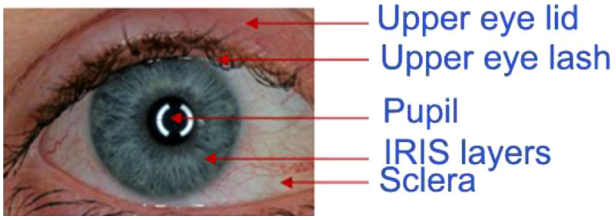

FIGURE 1 Eye image

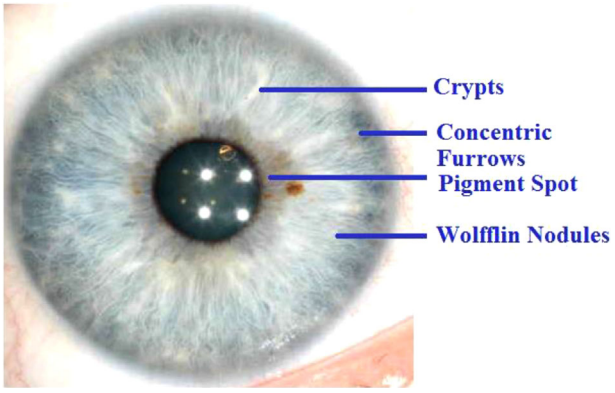

FIGURE 2 Iris biological features

eyelids. The image of the eye has to be captured and recorded during when the eye is in fully opened condition, which would give better results.

The iris consists of various features such as crypts, concentric furrows, wolfflin nodules, and pigment spots as shown in Figure 2. The upper and lower side features are affected by the eye laze and lids. The iris features are the combination of biological structures. The pigment spot is near to pupil. The crypts are broad in iris layer. Wolfflin nodules are between crypts and furrows. The furrows are located near the iris boundary.

2 | LITERATURE REVIEW

Histogram equalization and contrast-limited adaptive histogram equalization approaches were used by Maheshan [1] to visualize blurred sclera. Further segmentation was performed using the K-means and fuzzy C-means algorithms. Alkassar et al. [2] proposed a seed base initialization and snake-edge model for detecting iris boundaries. The segmented scleral features were enhanced for identification by separating the red, green, and blue layers. The green layer had more features. Isotropic undecimated wavelet features were extracted from the enhanced green layer of the image. The extracted features were then recognized using template matching.

Otsu's threshold-based scleral layer identification was proposed by Das et al. [3]. The red green blue (RGB) input image in the proposed algorithm was converted into YC_rC_b. The C_r component contained more valid information. Histogram equalization was performed on the Cr portion of the image. Otsu's thresholding is applied to the histogram equalized image, which provided the mask for eyelashes and eyelids during phase-1 processing. Otsu's thresholding was directly applied to the histogram equalized input image, which created the mask eye image except for the sclera part. The Gabor filter was further applied to the sclera. However, this method required improvement in the area of removal of eyelashes and eyelids.

A grey-level difference-based iris feature extraction method was proposed by Ahmadi [4]. The author used the Chinese Academy of Science, Institute of Automation (CASIA) V3 dataset. Barpanda et al. [5] proposed iris recognition based on the Mel-frequency coefficients. Iris segmentation was performed using the templates. The CASIA V3 and Indian Institute of Technology Delhi (IITD) databases were used. Rajput et al. [6] proposed a fusion radon multiwavelet transform-based iris feature extraction technique. The circular Hough transform (CHT) technique was used to segment the iris. This method achieved a recognition rate of 86.05%. Devi [7] proposed an iris-recognition algorithm for twins. The author used the CASIA V-4 dataset to test this method.

A template-based iris segmentation approach was used in the algorithm. Li et al. [8] proposed a robust iris-recognition method. Gaussian mixture model (GMM)-based segmentation was used in the method, and features were extracted using a convolutional neural network (CNN). The authors used the CASIA Iris 1000 database. Hofbaueet et al. [9] proposed a CCN-based iris recognition feature-segmentation algorithm. The circular segmented iris was converted into a rectangular form using the rubber sheet approach. Kumar et al. [10] proposed an algorithm for detecting liveness in the iris. The iris textures were extracted using Gaussian filters and *k*-means clustering. Circular disk template-based pupil detection was proposed by Kumar et al. [11]. The author had worked on the IITD Multimedia University (MMU) dataset images. The gradient descent approach was used to extract features.

Lv et al. [12] proposed a 2D log Gabor filter for extracting iris features. Recognition was performed using the Hamming distance between the pixels. Ouabidaet et al. [13] proposed an active contour-model-based iris boundary-detection approach. The method included filters and disc templates to detect the iris boundary and was tested using the CASIA, MMU, and Western Virginia University (WVU) dataset images. 1 D log Gabor and Fearnet feature-based segmentation were proposed by Wang et al. [14]. The algorithm was trained and tested using the CASIA V-4, Mobile Iris Challenge Evaluation -I (MICHE-I), and UBIRS V-2 datasets. The equal error rate (EER) of the proposed method varied from 2.7% to 11.2% depending on the database.

Zhang et al. [15] proposed a robust iris segmentation using U-Net and a dilated convolution approach. The algorithm used the CASIA V-4 and UBIRIS V-2 datasets for testing. Liu et al. [16] proposed a high-learning-rate network and pairwise filters to recognize iris features. The author of the proposed work had developed an algorithm to find the pupil and iris boundary with the highest accuracy rate [17]. The authors also developed a multiple left-right point (MLRP) algorithm for detecting pixels in the iris boundary using the visible iris region [18]. There have been many studies applying deep learning, such as CNN

to classification for disease diagnosis [19–21]. Matten et al. [22] proposed diabetic retinopathy (DR) detection using a CNN. The retina is located in the interior of the eye. DR affects human vision. Exudate is the DR feature used to determine the level of disease. Region of interest based augmentations were applied and CNN-based feature extraction was used.

In already existing works, instead of preprocessing, the raw eye images are fed into Alexnet for feature extraction and classification. The extracted feature of existing system consists of iris features and iris occultation's such as eye laze and lids. Due to this, the existing system's accuracy level is in the range of 95.63% to 98.6%. The computational time of the existing system also varies from 1.12 to 1.34 ms.

3 | MATERIALS AND PROPOSED METHODS

3.1 | Datasets

The iris recognition of the existing methods uses two stages: iris segmentation and feature extraction. The existing methods use iris templates, filters, and a CNN. Therefore, it is specific to certain database images, and hence the accuracy segmentation leads to reduced recognition accuracy. The feature extraction of existing methods uses a CNN and fully convolutional neural network (FCN).

The iris datasets used in the existing methods are collected from and cover various databases. These are open-source datasets; however, some providers may require the registration of researcher details to use the data. Registration forms have been made to have access to such data. The total number of images collected from all databases is 163,432. Specifically, we included the following datasets: CASIA V4, CASIA cross-sensor, CASIA IRIS 1000, UBIRIS V2, LG2200, Quality-Face/Iris Research Ensemble (Q-FIRE), and MICHE-I.

CASIA database images were collected from the Centre for Biometrics and Research [23]. The UBIRIS database images were collected from the University of Beria [24]. The LG2200 database was collected from the University of Notre Dame [25]. The Q-Fire datasets were collected from the National Institute of Standards and Technology, USA [26]. The MICHE-1 datasets were collected from the Biometrics and Image Processing Laboratory, University of Salerno [27].

The CASIA images were captured using Near InfraRed (NIR), Auto turn ON, and OFF lamp-enabled camera. The images were captured with distance varying from 0.5 to 3 m. The UBIRIS images were captured with the distance of 0.4 m. Q-Fire images were collected with the distance ranging between 0.127 and 0.635 m. The collected datasets were having non-ideal images, different resolutions, capturing image distance variations, and different lighting conditions. The data set access requests were raised with the corresponding data base providers. The datasets were downloaded from the link provided by the data base provider. The data bases are cited in the reference and utilized for research purpose as per the database usage agreement.

The biometric standards for verifying the proposed system with collected data sets are Accuracy, Sensitivity, Specificity, and F1-Score. The sensitivity specifies the Positive Prediction Accuracy of the system. The specificity gives the negative prediction accuracy of the system. The F1-score is performed using weighted average of positive prediction and negative prediction values. It is used to find the distribution dataset among positive and negative datasets.

3.2 | Proposed method

The proposed method is designed to detect the pupil boundary and centre in an eye image using a suitable filter and morphological operations. The iris boundary was identified using the reference pupil information and the MLRP algorithm. The iris location was segmented by excluding the pupil area using the parameters obtained from the MLRP. Deep learning AlexNet was modified and trained using the iris features. A comparative analysis was performed on choosing network solvers. The images were divided into training and testing categories. The AlexNet classifier was used to classify networks.

$$Gray_{Pix} = \frac{\left(R_{pix} + G_{pix} + B_{pix}\right)}{3} \tag{1}$$

$$Gray_{Pix} = \left(\left(0.21 \times R_{pix}\right) + \left(0.72 \times G_{pix}\right) + \left(0.07 \times B_{pix}\right)\right) \tag{2}$$

The proposed method consists of three stages. Stage-1 is used to detect the iris boundary. Stage-2 is used to extract iris features. Stage-3 is the recognition phase, which uses deep-learning networks. A block diagram of the proposed method is shown in Figure 3. The grey conversion was used to convert the RGB format of the image into greyscale. The grey level of the image was converted using the expression Equation (1). This method is also called the averaging method. The terms $\boldsymbol{R_{pix}}$, $\boldsymbol{Gpix}$, and $\boldsymbol{B_{pix}}$ represent the red, green, and blue values of the pixel, respectively. The $\boldsymbol{greypix}$ represents the equivalent greyscale value. The averaging method is not suitable for human eye-based processing systems. Therefore, the luminous-based method is prepared using the proposed algorithm, which is represented in Equation (2). The grey level of the 8-bit image varied in the range of 0 to 255.

A median filter was used as the pupil filter. The expression for the non-linear median filter is given by Equation (3), where Re_{pix} represents the median pixel value. The terms 'u,' 'n', and 'q' correspond to the input image, replaceable pixel, and a term derived from the filter tapping. The term 'q' derived from the filter tapping is given in Equation (4). The term 'N' represents the filter tap. The filter tap is an odd number. The filter values are 3, 5, 7, 9, 11 etc., and the conversion of the grey image to binary is achieved using the fixed thresholding method. The expression for fixed thresholding is given in Equation (5). The terms $y(r, c)$ and $x(r, c)$ represent the binary and input images, respectively. In the proposed algorithm, the filtered image is used as the input for the binary conversion process. A threshold value

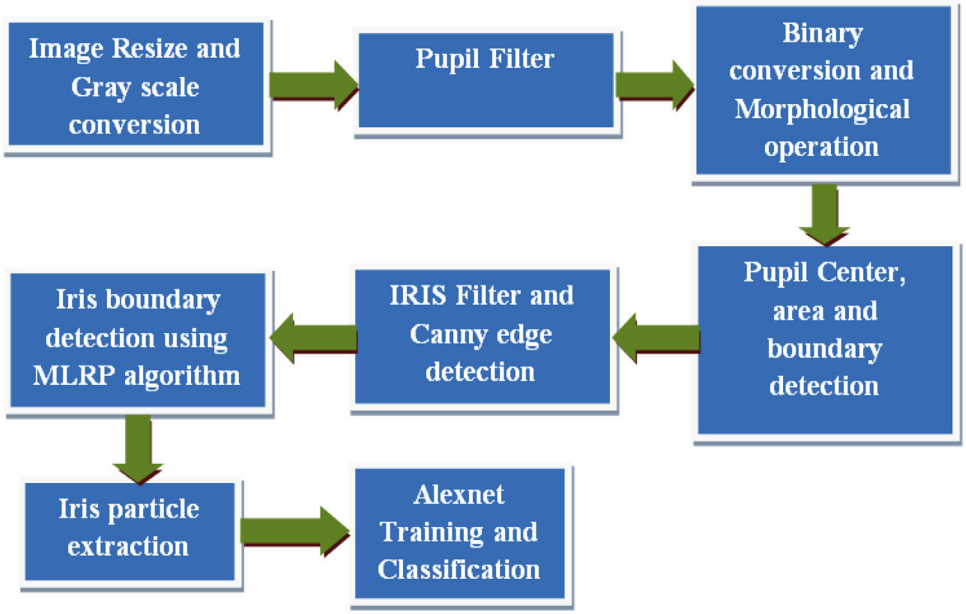

FIGURE 3 Block diagram of proposed method

(*Thres*) of 127 is fixed in the proposed algorithm to retain the pupil part. If the threshold value is greater than or equal to 127, the corresponding pixel is replaced by logic '1' [28].

$$Re_{pix}(n) = median_{pix}\begin{bmatrix} u(n-q), \\ u(n-q+1), \ldots u(n), \\ \ldots\ldots, u(n+q-1), \\ u(n+q) \end{bmatrix} \tag{3}$$

$$q = \frac{(N-1)}{2} \tag{4}$$

$$y(r,c) = \begin{cases} 0 \;\; if \;\; or \;\; else \\ 1 \;\; if \;\; x(r,c) \geq Thres \end{cases} \tag{5}$$

The morphological operation uses mathematical functions to identify the specific shapes of the elements. Initially, the pixels were structured using a strelite operation. This was the preliminary process required for erosion and dilation. The erosion process created a thin line over the structured element [29]. Dilation created a thicker line over the structured element. The erosion and dilation processes are expressed in Equations (6) and (7). The input image is 'P' and 'Q' is the structured element or strelite processed image. The term 'x' is the vector that is derived from 'Q_x'. 'Z' is the origin of the structured element. The morphological area's open and close operations are expressed in Equations (8) and (9). Open and closed areas are used to fill or remove structured pixels [30]. The border clear is another functionality to replace the logic '1' pixels near the border of the image. The complement of the image is obtained by using Equations (6) to (10).

$$P \Theta Q = \{x \in Z | Q_x \subseteq P\} \tag{6}$$

$$P \oplus Q = \bigcup_{q \in Q} P_q \tag{7}$$

$$P \circ Q = (P \Theta Q) \oplus Q \tag{8}$$

$$P \bullet Q = (P \oplus Q) \; \Theta Q \tag{9}$$

$$\overline{P}(x,y) = 1 - P(x,y) \tag{10}$$

Canny edge detection is based on a Gaussian filter. The expression for the Gaussian filter is given in Equation (11). The parameter 'A' is derived from the Equation (12). The parameter 'B' is derived from Equation (13). The term '*p*' defines the threshold value. The edge detector detects pixels greater than *p*. The term 'σ' defines the deviation of the filter with concern to the standard value. The row and column of the image are defined using the notations 'x' and 'y'. The Canny edge detector uses two types of thresholding: lower and upper threshold values. These are also called the local minimum and maximum threshold values. The term '$\mathbf{Z}_{Upper}$' is the upper threshold value and the lower threshold value is denoted by '$\mathbf{Z}_{Lower}$' The edge detector finds pixels that lie between the upper and lower threshold values. The relationship between the upper and lower threshold values of Canny is given in Equation (14).

$$Gaussian_{x,y} = \frac{1}{2\pi\sigma^2} \exp\left(-\frac{A^2+B^2}{2\sigma^2}\right) \tag{11}$$

$$A = x - (p+1) \tag{12}$$

$$B = y - (p+1) \tag{13}$$

$$Z_{Lower} = \frac{(10 \times Z_{Upper})}{25} \tag{14}$$

The MLRP algorithm was used to find the visible pixels of the iris boundary in the 180° and 360° positions [28]. The pupil 180° pixel location is identified using the mid-row position of the pupil boundary (x). The logic '1' pixel is searched in the direction of 180°. A column-wise search 'y' is performed. The search is completed when the logic '1' pixel is cornered. The cornered logic '1' pixel is recorded. The initial value of 'x' is incremented by the numerical value '1' and the above procedures are repeated to find more pixels in quadrant-II of the iris boundary. The initial value of 'x' is reloaded and decremented by the numerical value '1' and the Identify_left_position procedure is followed by more pixels in quadrant-III of the iris boundary. The iris pixels near 360° in quadrants I and IV are identified using the procedure identify_right_position. The MLRP results are around a 30-pixel location near 180° and 360° of the iris boundary. Iris boundary pixels near 180° and 360° are detected. The distances between the pixels (Dist) are measured using Equation (15). This is used to determine the diameter of the iris boundary. (X, Y) represents the pixel in the 180° direction, and (P, Q) represents the pixel in the 360° direction. The (X, Y) locations lie in quadrants II and III, respectively. The (P, Q) locations lie in quadrants I and IV, respectively.

$$Dist\left((X,Y),(P,Q)\right)=\sqrt{\left((X-P)^2+(Y-Q)^2\right)} \tag{15}$$

$$Pixel_{Shift}=\begin{cases}\left|Q(i+1)-Q(i)\right|\neq 0\\ \left|Y(i+1)-Y(i)\right|\neq 0\end{cases} \tag{16}$$

$$Z[i]=Pixel_{Shift}\{X_i,.....X_n\} \tag{17}$$

$$Iris_{180°}[X]=Iris_{360°}[P]=Z\left[Round\left(\frac{n}{2}\right)\right] \tag{18}$$

$$Iris_{Center}[Column]=\left(\frac{\left(Iris_{360°}[Q]-Iris_{180°}[Y]\right)}{2}\right) \tag{19}$$

$$Iris_{Center}[row]=Iris_{180°}[X] \tag{20}$$

$$Iris_{Dia}=Dist\left((X_{180°},Y_{180°}),(P_{360°},Q_{360°})\right) \tag{21}$$

$$Iris_{radius}=\frac{Iris_{Dia}}{2} \tag{22}$$

The column shifting of the iris boundary pixel can be identified using Equation (16). The value of 'i' is the value of the array. The terms 'Y and 'Q' are the column values of iris boundary pixels. The zero shifting row values were computed using the expression given in Equation (17). The term 'n' is the total number of zero shift locations. The 180° and 360° iris row values were computed using Equation (18). The iris centre row and column values were computed using Equations (19) and (20). The iris diameter and radius were calculated using Equations (21) and (22). These procedures were used to accurately determine the iris boundary in the eye. The scleral top and bottom areas may spread to the eyelids and eyelashes. Eyelash was the most dominant noise spreading feature in the sclera.

The combination of iris particles consists of crypts, contraction furrows, pigment spots, and Wolffin nodules. The Wolffin nodule is located near the iris boundary. The eyelashes, eyelids, and closing of the eye position may hide some of the Wolffin nodules. Squared blocks were segmented within the iris. The square blocks extracted from the images were stacked into separate folders. The folder consists of image features. These images were trained using a CNN. Many deep learning pre-trained networks are available. The pre-trained networks are squeeze net, Google Net, Resnet-50, Darknet-53, Darknet-19, Shuffle Net, NasNet-mobile, NasNet-large, Xception, Places365-Google, MobileNet-v2, DenseNet-201, ResNet-18, Inception-ResNet, Inception-v3, ResNet-101,VGG-19, VGG-16, and AlexNet [31].

The proposed work uses an AlexNet multilayered deep learning network based on the results of Tobji et al. [18]. The AlexNet architecture is shown in Figure 4. The AlexNet significantly consists of five convolution filter layers, two normalization layers, seven linear rectified layers [37]. The layers are the input layer, convolution layer-1(conv-1), linear rectified unit-1(ReLu-1), Cross Channel Nominalization-1(norm-1), max polling-1(pool-1), grouped convolution-2(conv-2), ReLu-2, norm-2, pool-2, conv-3, ReLu-3, conv-4, ReLu-4, conv-5, ReLu-5, pool-5, Fully connected-6(FC-6), ReLu-6, Drop Out-6(drop-6), FC-7, ReLu-7, drop-7, FC-8, softmax (Prob), and output layer. The initially segmented features of the iris were divided into training and test images. The training and test images were randomly selected at a ratio of 7:3.

The pre-trained Alex network was loaded, and the input required was 227 × 227 × 3. The input images were to be resized to 227 × 227 × 3 as per the requirement of AlexNet architecture. The AlexNet end three layers were modified according to the iris image classes. Each class consisted of a set of iris features. The layers are fully connected -8(FC-8) (layer-23), softmax layer (layer-24), and output layer (layer-25). The training and test images were resized to 227 × 227 pixels according to the network input requirements. The process was performed using data augmentation. The layers before 24 need to be trained according to the modification in the final three layers of Alex. The layers are trained using various solvers, such as stochastic gradient descent with momentum (SGDM), squared decaying factor (ADAM), average gradient decay factor (GDF), and SGDF [38]. The proposed work prefers a solver based on the accuracy of the IRIS features.

4 | RESULTS AND DISCUSSION

The proposed system needs to be tested and compared with the existing method. It is required to understand the effectiveness of proposed research work. The test and trained image of the proposed method are 49,030 and 114,402, respectively. The total number of images used in the proposed method is 163,432 eye images. The total images are divided into 49,030 test images and 114,402 trained images. The images are from CASIA V-4, CASIA Iris 1000, LG2200, UBIRIS V-2, CASIA cross sensor, Q-Fire, and MICHE-I database images. The proposed method

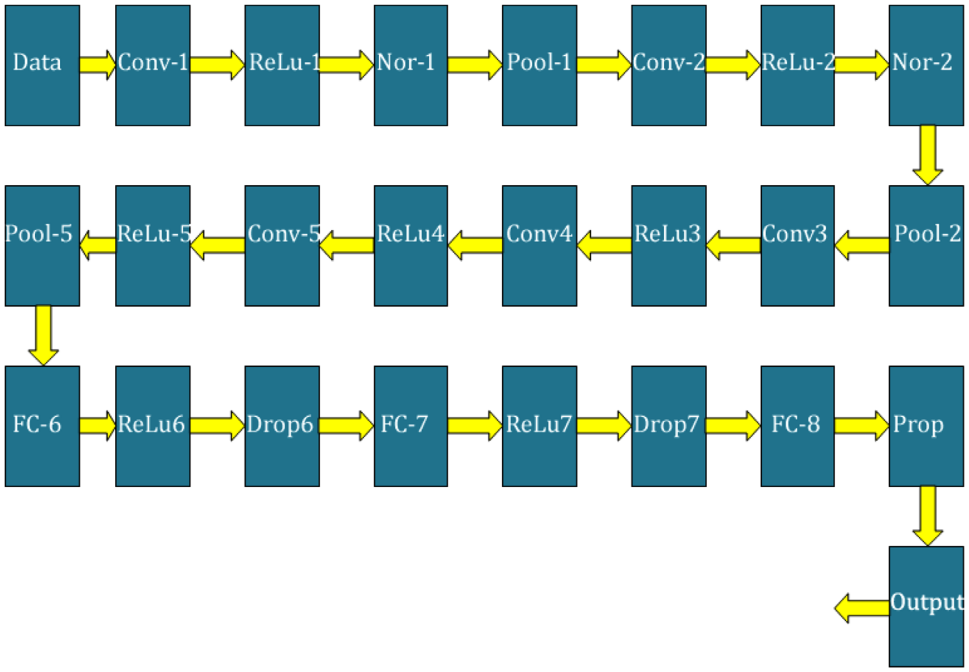

FIGURE 4 Block diagram of multilayer deep learning AlexNet

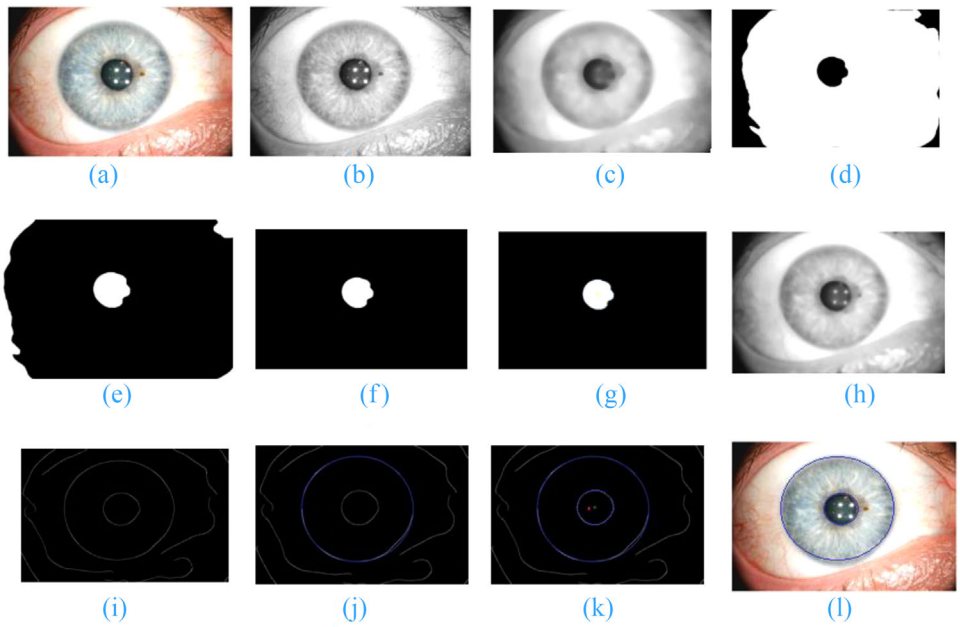

FIGURE 5 Iris boundary detection

is trained and tested using the Dual core i3 Processor with the speed of 2 GHz, and 8GB RAM.

The uniqueness of the proposed work starts with the identification of the accurate boundaries of the iris. The stage-by-stage output of the iris boundary detection is shown in Figure 5. The input image is shown in Figure 5a. It is the left eye. The eye image consisted of the upper and lower eyelids, eyelashes, iris, pupil, and sclera. The proposed algorithm treats the eyelashes, eyelids, and complete iris portions as noise. The given input image was converted into a greyscale image, and the corresponding output is shown in Figure 5b. The grey level of the image varied from 0 to 255. The greyscale images were subjected to a median filter with a masking window of 25 × 25 pixels. The image appeared blurred, as shown in Figure 5c. The 25 × 25 masking window gives the clear view of pupil. The mask values below the 25 × 25 may give more information about iris

boundary in addition to pupil boundary. The 25 × 25 mask window gives exact pupil area. The value greater than 25 × 25 will lead to loss of pupil area. The blurring effect occurs in the eyelashes, eyelids, sclera, and iris. However, there were no changes in the iris and pupil regions. The filtered image was converted into a binary image with a threshold value of 128, and the results are shown in Figure 5d.

The grey levels below 128 are converted into '0'and above 128 are converted into logic '1'. The pupil portion appeared and filled up with black pixels. The portions such as sclera, iris (except pupil), and upper and lower eyelashes are removed in the binary processing. The binary image is applied with morphological operations such as area open, dilation, and the area close to the circle. The morphologically progressed image is complemented and shown in Figure 5e. The complemented image is further subjected to border clear operation and the corresponding result is shown in Figure 5f. The white pixels near the corner are replaced by black pixels. The output clearly shows the pupil part in terms of white pixel background. The region property operation is applied with the filter of disk position. It finds the area and the centre position of the pupil as shown in Figure 5g.

Now, the pupil centre and boundary appeared. To obtain the iris boundary, the median filter is applied again on the grey-scaled input image with a masking of 15 × 15, and the result is shown in Figure 5h. The sclera, iris, and pupil positions were obtained more clearly than for the first stage filter. Canny edge detection is applied to the stage II filtered image with a Canny upper threshold value of 20. The corresponding results are shown in Figure 5i. If the edge detector threshold is less than 17, inner particles appear between the pupil and iris. If the threshold value is greater than 20, iris boundary information is lost. Therefore, the threshold value of 20 was fixed in the proposed method.

The left and right boundary positions of the iris boundary were located using the MLRP algorithm with concern to the pupil centre and boundary. The centre pixel location was identified using Equations (15) and (19). The diameter and radius of the iris boundary were computed using Equations (20) and (21). The corresponding results are shown in Figure 5j. The identified pupil and iris boundaries are marked on the edge-detected eye image, as shown in Figure 5k. This indicates that the centres of the pupil and iris boundaries are not the same. In some images, the centres were the same. The iris and pupil boundaries were marked in the input image, and the corresponding outputs are shown in Figure 5l.

Table 1 shows a sample of five eye images. The table parameters were used to provide the boundary line for extracting iris features, excluding the pupil and other eye parts. The IRIS features were extracted in a rectangular form within the iris boundary. The pupil and iris diameters were a combination of pixels in the diameter line.

The iris is a combination of concentrated furrow pigment spots, wolflin nodules, and crypt layers. The iris features were segmented from the eye image within the boundary limits using the Table 1 parameters. A sample of the segmented features is presented in Figure 6. The features show iris features excluding the pupil. This covers the entire region of the iris boundary. In

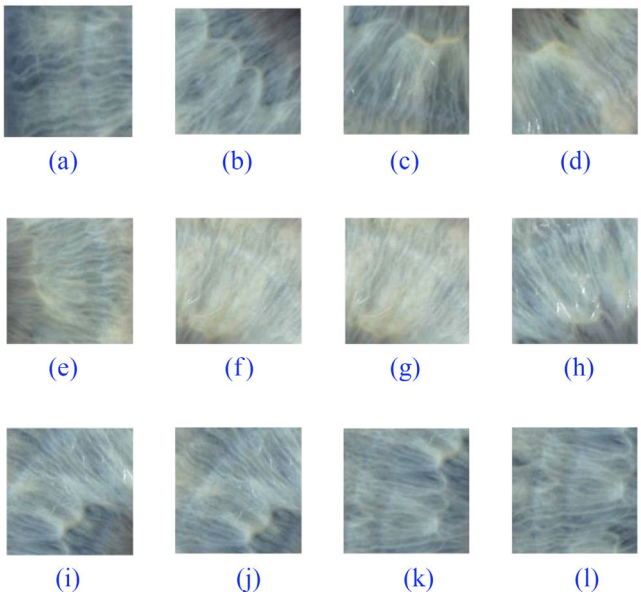

FIGURE 6 Segmented IRIS features of img_1

12 outputs, 12 samples of features are shown in the output. The outputs shown in Figure 6a and 6f are feature extraction in combination with crypts and contraction furrows. The combination of crypts, pigment spots, and concentrated furrows is shown in Figures 6g, 6h, 6i, and 6j. Pure crypt features were extracted, as shown in Figure 6e. Combinations of pigment spots and crypts are shown in Figures 6b, 6c, and 6d. The combination of wolflin nodules, crypts, and concentrated furrows is shown in Figure 6l. The features were extracted using rectangular coordinates. The rotational-invariant problem is inconsistent with the proposed method.

The dataset used in the proposed method and the distribution among training and test categories are shown in Table 2. The images were randomly distributed using a random distribution toolset. There are three types of datasets from CASIA: cross-sensor, Version-4, and iris-1000. The LG 2200 dataset consisted of approximately 116,564 iris images. The Q-Fire dataset consisted of 3008 images, of which 2106 and 902 were taken as the training and test distributions, respectively. The MICHE-I dataset images were divided into 2234 and 957 images for training and testing, respectively. The total number of images used in the proposed method was 163,432. The numbers of training and test images were 114,402 and 49,030, respectively. The image size of CASIA V-4 is 320 × 280. The image size of LG2200, CASIA cross sensor, Q-Fire, and MICHIE-I is 640 × 480. The image size of UBIRIS V2 is 400 × 300.

The segmentation accuracy of the proposed system was compared with that of the existing method, as shown in Figure 7. The segmentation accuracy is important for achieving better feature extraction. The execution error was compared with the 1-D log Gabor and Fear-net methods proposed by Wang et al. [14]. The proposed method showed smaller errors of 1.79%, 8.69%, and 4.6%, respectively, for CASIA V-4, MICHE-I, and UBIRIS-V2 datasets.

TABLE 1 IRIS and pupil boundary parameters

Image name	MLRP attained parameter		Diameter of pupil	Centre pixel position of pupil	Diameter of iris	Centre pixel position of the iris
	180° pixel position	360° pixel position				
Img_1	226, 166	226, 550	26	226, 364	384	226, 358
Img_2	189, 98	189, 400	21	188, 246	302	189, 249
Img_3	180, 141	180, 397	18	180, 310	255	180, 308
Img_4	165, 221	165, 381	17	166, 326	160	165, 325
Img_5	167, 84	167, 348	18	168, 214	264	167, 216

TABLE 2 Datasets and distribution of proposed method

S. No	Data set	Training	Test	Total
1	CASIA V-4 [23]	1797	770	2567
2	CASIA Iris 1000 [23]	14,000	6000	20,000
3	LG2200 [25]	81,595	34,969	116,564
4	UBIRIS V-2 [24]	7771	3331	11,102
5	CASIA cross sensor [23]	4900	2100	7000
6	Q-Fire [26]	2106	902	3008
7	MICHE-I [27]	2234	957	3191
Total		114,402	49,030	163,432

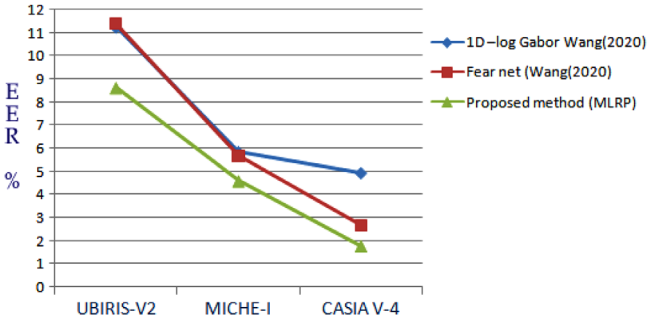

FIGURE 7 Segmentation performance analysis

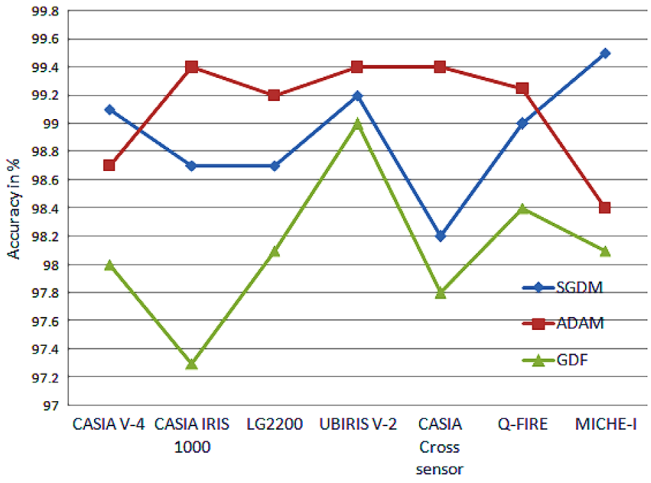

FIGURE 8 AlexNet solver analysis

The images were loaded and converted to 227 × 227 × 3 pixels, which is acceptable for the Alex network. The final three layers of AlexNet were modified according to the database classes given in Table 3. AlexNet layers 2 to 23 were trained using three different solvers, and their accuracies were compared. Table 3 shows that the ADAM solver provides higher accuracy for CASIA IRIS 1000, LG2200, UBIRIS V-2, and Q-Fire. The SGDM method provided lead accuracy for the CASIA V-4 and MICHE-I datasets.

An analysis of the AlexNet training solver is shown in Figure 8. The GDF solver provided less accuracy for all the datasets. However, it achieved a minimum accuracy of 97.3% for CASIA IRIS 1000 dataset. The accuracy levels of SGDM and ADAM were the same with almost nearest values. This shows that the difference in accuracy is within 0.5%. In most datasets, ADAM leads slightly, compared with SGDM. Therefore, either the ADAM or SGDM can be used to train the network. This complete database was trained and validated by using the ADAM solver to compute the overall accuracy of the system.

The training and testing accuracies obtained for the network are shown in Figure 9. The network was trained and validated under the minimum and maximum epochs of 8 to 30. The accuracy is above 80% after the second epoch. The accuracy level is above 95% after the fifth epoch. The training and test images show a perfect fit after the 10th epochs. It shows that the system requires a minimum of 10 epochs to get higher accuracy. Epochs may increase till 30 for getting higher accuracy and again depends on the selected data base images. The epochs above 30 will lead to the deviation in the train and test images and also reduce the accuracy level. In the above analysis, for a particular image at the 11th epoch, the accuracy level is high and at 12th epoch onwards the accuracy level gets decreased. It shows that the iris images with AlexNet architecture will give the perfect fit at the 11th epoch. The proposed method achieved an overall accuracy of 99.1%, including the entire database.

The proposed method used various database images. The accuracies of the proposed system are listed in Table 4. The true positive, true negative, false positive, and false negative were

TABLE 3 Accuracy assessment based on training solvers of AlexNet

Solver	CASIA V-4	CASIA IRIS 1000	LG2200	UBIRIS V-2	CASIA cross sensor	Q-FIRE	MICHE-I
SGDM	99.1%	98.7%	98.7%	99.2%	98.2%	99%	99.5%
ADAM	98.7%	99.4%	99.2%	99.4%	99.4%	99.25%	98.4%
GDF	98%	97.3%	98.1%	99%	97.8%	98.4%	98.1%

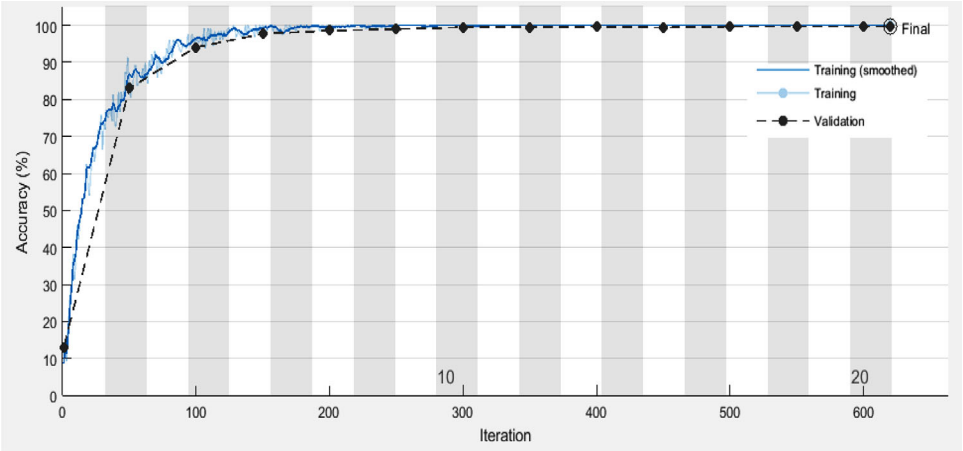

FIGURE 9 AlexNet work training and validation

TABLE 4 Proposed method accuracy analysis

S. no	Data base	Trained images	Test images	True positive (TP)	True negative (TN)	False positive (FP)	False negative (FN)	Accuracy $\left(\frac{(TP+TN)}{TP+TN+FP+FN}\right)$
1	CASIA V-4 [23]	1797	770	1774	761	23	9	98.7
2	CASIA Iris 1000 [23]	14,000	6000	13,929	5970	71	30	99.4
3	LG2200 [25]	81,595	34,969	81,014	34,705	581	264	99.2
4	UBIRIS V-2 [24]	7771	3331	7730	3315	41	16	99.4
5	CASIA cross sensor [23]	4900	2100	4876	2083	54	17	99.4
6	Q-Fire [26]	2106	902	2093	893	13	9	99.25
7	MICHE-I [27]	2234	957	2206	936	29	21	98.4
Total images		114,402	49,030	113,622	48,663	812	366	99.2

computed using trained images, test images, and authorized and unauthorized classifications. The TP refers to the number of valid images identified as true. The TN refers to the number of invalid images identified as false. The FP refers to the number of invalid images identified as true. The FN refers to the number of valid images identified as negative. The CASIA IRIS 1000 [23] data base in Table 4 is used for explanation. The number of trained and test images from the data base is 14,000 and 6000, respectively. The proposed system identifies TP as 13,929, TN as 5970, FN as 71, and FN as 30. The accuracy obtained on CASIA IRIS 100 database with the proposed method is 99.4%. The classification was performed manually and cross-verified using a simulation. The numbers of trained images, test images, TP, TN, FP, and FN of the images were 114,402, 49,030, 113,622, 48,663, 812, and 366, respectively. The accuracy of the proposed system is 99.2. The total number of true positives was 113,622 using the Alexnet with ADAM solver.

The performance of the proposed system is analyzed using sensitivity, specificity, and F1-score and the corresponding numeric scores are shown in Table 5. For CASIA V4, IRIS 1000, the cross-sensor sensitivity varies from 99.5% to 99.79%. The MICHI-1 data base sensitivity is 99.06%. For CASIA V4, IRIS 1000, the cross-sensor specificity varies from 97.07% to 98.82%. The MICHI-1 data base specificity is 96.99%.

TABLE 5 Comparison of proposed system accuracy with existing methods

S. no.	Data base	Sensitivity % $\frac{(TP)}{(TP+FN)}$	Specificity % $\frac{(TN)}{(TN+FP)}$	F1-score $\frac{TP}{TP+\frac{(FP+FN)}{2}}$
1	CASIA V-4 [23]	99.50	97.07	0.991
2	CASIA Iris 1000 [23]	99.79	98.82	0.996
3	LG2200 [25]	99.68	98.35	0.995
4	UBIRIS V-2 [24]	99.79	98.78	0.996
5	CASIA cross sensor [23]	99.65	97.47	0.993
6	Q-Fire [26]	99.57	98.57	0.995
7	MICHE-I [27]	99.06	96.99	0.989
Overall		99.68	98.36	0.995

TABLE 6 Comparison of proposed system accuracy with existing methods

Data base	CASIA-1000	LG2200	UBIRIS-Ver-2	CASIA- V4	Q-Fire	CASIA cross sensor
Tobji et al. [18]	95.63%	93.17%	99.41	–	–	–
Bazrafkan et al. [33]	99.3%	–	94.9%	–	–	–
Nguyen et al. [34]	98.8%	98.7%	–	–	–	–
Zhao et al. [32]	–	–	–	96.15%	–	–
Liu et al. [16]	–	–	–	–	98.85%	98.69%
Arsalan et al. [36] (DenseNet)				99.14		
Liu et al. [35](condensed CNN)				98.81%		
Sun et al. [38]		98.5%				
Proposed method	99.4%	99.2%	99.4%	98.7%	99.25%	99.4%

The overall sensitivity and specificity are 99.68 and 98.36, respectively. The specificity is 1.36% lesser than the sensitivity. The overall F1-Score of 0.995 is a good value and shows the distribution of positive and negative values at uniform rate.

The proposed method was trained and tested on a wide range of datasets. Table 6 shows the results of the proposed method compared with the existing methods, carried out by various researchers. The proposed method achieved 99.4% accuracy on the CASIA IRIS 1000 dataset, which is closer to the method proposed by Nguyen et al. [34]. The accuracy of the LG2200 data set is 99.2%, and 0.5% greater than the method proposed by Nguyen et al. [34] and 6% greater than that achieved by Tobji et al. [18]. The accuracy of UBIRIS V-2 is 99.4%, which is comparatively equal to Tobji et al. [18], and also 4.5% greater than Bazarafkan et al. [33]. The accuracy of the CASIA V4 data set is 98.7%, which is 2.55% greater than the method proposed by Zhao et al. [32]. The proposed method's accuracy obtained on Q-Fire and CASIA cross-sensor datasets is 99.25% and 99.4%, respectively, which is more than 1% greater than the method proposed by Liu et al. [16]. The accuracy level of the proposed method closely matches with that of DenseNet and condensed CNN.

The deep learning networks give a close level of accuracy. Therefore, the timing complexity is performed and compared in Table 7. The images are trained and tested using other deep learning networks such as DenseNet, ResNet, and VGG. Fluctuation in accuracy is observed while using a wide range of databases. The Alexnet will give a higher degree of accuracy to proposed images. The deep learning network accuracy of others was found to be decreased on proposed images. The timing complexity is also computed for the proposed system. The average execution time of the images is shown in Table 6. The proposed method's overall computation time from input image to authentication is 1.01 ms which is slightly less than DenseNet and CNN for the Img_1. Therefore, the proposed system used the AlexNet for covering a wide range of databases. If the system is adopted using the proposed method it could cover the real images in a different environment.

5 | CONCLUSION AND FUTURE WORK

The proposed method was applied to iris recognition systems using precise segmentation and an AlexNet deep learning multilayer network. The segmentation process includes the initial detection of the pupil boundary. The MLRP algorithm was used to detect the iris boundary and the centre. Many images used in the database have different types of pupil and iris centres. The total number of images used is 163,432 which includes

TABLE 7 Timing complexity analysis

Data base	Technique	Augmentation	Computational time
Arsalan et al. [34]	DenseNet	Nil	1.34 ms
Liu et al. [35]	Condensed CNN	Brightness, shifting, and scaling	1.12 ms
Proposed method	AlexNet	MLRP, median filter, and morphological operations	1.01 ms

the trained and test images. The proposed system achieved a segmentation accuracy of 98.21 %. The datasets were trained using AlexNet with an ADAM solver. The AlexNet with ADAM solver achieved a system accuracy of 99.1% on all dataset images. The proposed system covers various dataset images, such as CASIA IRIS 1000, CASIA V-4, CASIA cross sensor, LG2200, Q-Fire, and MICHE-I. The proposed work was trained and tested using 163,432 iris images from seven standard eye data bases. The data base selection was done based on the methods found in the literature work. The images were of different resolutions which were supported by the proposed system. The proposed work uses the preprocessing stage which helps to find the clear iris boundary. An automated cropping parameter extracts iris area which excludes iris noise occultation. The clear iris feature is finally extracted using the proposed system. There are multiple features that are extracted to separate the iris. The features are trained and classified using Alexnet. It helps the proposed system to reach a high accuracy level of 99.2% and also reduces the computational time to 1.01 ms. The F1-score of the proposed system is in the scale of 0.995. It shows the uniform distribution of images among positive and negative levels.

Future work: The proposed work is performed using cross compiler mode. In order to implement the proposed system in real time, the suitable hardware is required. The input images are to be captured using a camera. The size of camera captured image has to be reduced in accordance with the proposed algorithm.

AUTHOR CONTRIBUTIONS

Thiyaneswaran Balashanmugam: Conceptualization; Data curation; Formal analysis; Methodology; Writing – original draft; Writing – review & editing. Kumarganesh Sengottaiyan: Conceptualization; Data curation; Formal analysis; Software; Visualization; Writing – original draft. Martin Sagayam Kulandairaj: Methodology; Resources; Supervision; Validation; Writing – original draft; Writing – review & editing. Hien Dang: Conceptualization; Funding acquisition; Methodology; Project administration; Writing – original draft; Writing – review & editing.

ACKNOWLEDGEMENTS

We would like to thank all of our universities for facilitating our time support in this study.

CONFLICT OF INTEREST

The authors declare that we have no conflict of interest.

DATA AVAILABILITY STATEMENT

The datasets used in this study are available from the link indicated in the paper or from the corresponding author upon reasonable request.

REFERENCES

1. Maheshan, M.S., Harish, B.S., Nagadarshan, N: On the use of image enhancement technique towards robust sclera segmentation. Procedia Comp. Sci. 143, 466–473 (2018)
2. Alkassar, S., et al.: A. robust sclera recognition system with novel sclera segmentation and validation techniques. IEEE Trans. Syst. Man Cybern. Syst. 47(3), 474–486 (2017)
3. Das, A., et al.: SSERBC 2017: Sclera segmentation and eye recognition benchmarking competition. In: IEEE International Joint Conference on Biometrics (IJCB), pp. 742–747 (2017)
4. Ahmadi, N., Akbarizadeh, G.: Iris tissue recognition based on GLDM feature extraction and hybrid MLPNN-ICA classifier. Neural Comput. Appl. 32, 2267–2281 (2020) https://doi.org/10.1007/s00521-018-3754-0
5. Barpanda, S.S., et al.: Iris feature extraction through wavelet mel-frequency cepstrum coefficients. Opt. Laser Technol. 110, 13–23 (2019). https://doi.org/10.1016/j.optlastec.2018.03.002
6. Rajput, M.R., Sable, G.S., Gite, H.R.: Iris biometric technique for person authentication based on fusion of radon and 2D multi-wavelet transform. In: 2018 International Conference on Advances in Communication and Computing Technology (ICACCT) (2018). https://doi.org/10.1109/icacct.2018.8529514
7. Devi, C.N.: Automatic segmentation and recognition of iris images: With special reference to twins. In: 2017 Fourth International Conference on Signal Processing, Communication and Networking (ICSCN), pp. 1–5 (2017). https://doi.org/10.1109/ICSCN.2017.8085415
8. Li, Y.H., Huang, P.J., Juan, Y.: An efficient and robust iris segmentation algorithm using deep learning. Mobile Inform. Syst. 2019, 4568929 (2019). https://doi.org/10.1155/2019/4568929
9. Hofbauer, H., Jalilian, E., Uhl, A.: Exploiting superior CNN-based iris segmentation for better recognition accuracy. Pattern Recognit. Lett. 120, 17–23 (2019). https://doi.org/10.1016/j.patrec.2018.12.021
10. Kumar, M., Puhan, N.B.: Iris liveness detection using texture segmentation. In: 2015 Fifth National Conference on Computer Vision, Pattern Recognition, Image Processing and Graphics (NCVPRIPG) (2015). https://doi.org/10.1109/ncvpripg.2015.7490042
11. Kumar, J.R.H., Teotia, K.: Automatic pupil segmentation based on circular active discs. In: 2019 IEEE Region 10 Conference (TENCON), pp. 1932–1936 (2019). https://doi.org/10.1109/TENCON.2019.8929672
12. Lv, L., Yuan, Q., Li, Z.: An algorithm of Iris feature-extracting based on 2D Log-Gabor. Multimed. Tools Appl. 78(16), 22643–22666 (2019). https://doi.org/10.1007/s11042-019-7551-2
13. Ouabida, E., Essadike, A., Bouzid, A.: Optical approach for iris segmentation and tracking. In: 2016 4th IEEE International Colloquium on Information Science and Technology (CiSt), pp. 476–480 (2016), https://doi.org/10.1109/CIST.2016.7805095
14. Wang, C., et al.: Towards complete and accurate iris segmentation using deep multi-task attention network for non-cooperative iris recognition. IEEE Trans. Inf. Forensics Secur. 15, 2944–2959 (2020). https://doi.org/10.1109/TIFS.2020.2980791

15. Zhang, W., et al.: A robust iris segmentation scheme based on improved U-net. IEEE Access 7, 85082–85089 (2019). https://doi.org/10.1109/ACCESS.2019.2924464
16. Liu, N., et al.: DeepIris: Learning pairwise filter bank for heterogeneous iris verification. Pattern Recognit. Lett. 82, 154–161 (2016). https://doi.org/10.1016/j.patrec.2015.09.016
17. Thiyaneswaran, B., Kandiban, R., Jayakumar, K.S.: Elimination of iris hazards intended for localization using visible features for IRIS region. Proc. Eng. 38, 246–252 (2012)
18. Tobji, R., Di, W., Ayoub, N.: FMnet: Iris segmentation and recognition by using fully and multi-scale CNN for biometric security. Appl. Sci. 9, 2042 (2019). https://doi.org/10.3390/app9102042
19. Elayaraja, P., et al.: An efficient approach for detection and classification of cancer regions in cervical images using optimization based CNN classification approach. J. Intell. Fuzzy Syst. 43(1), 1023–1033 (2022). https://doi.org/10.3233/JIFS-212871
20. Naveen Sundar, G., et al.: Automated sleep stage classification in sleep apnoea using convolutional neural networks. Inform. Med. Unlocked. 26, 100724 (2021). https://doi.org/10.1016/j.imu.2021.100724
21. Andrushia, A.D., et al.: Visual-saliency-based abnormality detection for MRI brain images—Alzheimer's disease analysis. Appl. Sci. 11(19), 9199 (2021). https://doi.org/10.3390/app11199199
22. Mateen, M., et al.: Exudate detection for diabetic retinopathy using pretrained convolutional neural networks. Complexity 2020, 1–11 (2020). https://doi.org/10.1155/2020/5801870
23. CASIA Iris Image Database. http://www.cbsr.ia.ac.cn/english/IrisDatabase.asp. Accessed 12 Aug 2021
24. UBIRIS Image Database. http://iris.di.ubi.pt/. Accessed 12 Aug 2021
25. LG2200 Image Database. https://cvrl.nd.edu/projects/data/#nd-crosssensor-iris-2012-data-set. Accessed 12 Aug 2021
26. Q-Fire Image Database. https://www.nist.gov/document/irexiipublicreleasezip. Accessed 12 Aug 2021
27. MICHE-1 Image Database. http://biplab.unisa.it/MICHE/database/. Accessed 12 Aug 2021
28. Thiyaneswaran, B., Kandiban, R., Jayakumar, K.S.: Localization of iris region using MLRP algorithm intended for biometric applications. Eur. J. Sci. Res. 74(1), 126–133 (2012)
29. Thiyaneswaran, B., et al.: Early detection of melanoma images using gray level co-occurrence matrix features and machine learning techniques for effective clinical diagnosis. Int. J. Imag. Syst. Technol. 31, 682–694 (2021). https://doi.org/10.1002/ima.22514
30. Kumarganesh, S., Suganthi, M.: An enhanced medical diagnosis sustainable system for brain tumor detection and segmentation using ANFIS classifier. Curr. Med. Imag. Rev. 14(2), 271–279 (2018)
31. Kumarganesh, S., Suganthi, M.: An efficient approach for brain image (tissue) compression based on the position of the brain tumor. Int. J. Imag. Syst. Technol. 26(4), 237–242 (2016)
32. Zhao, Z., Kumar, A.: Towards more accurate iris recognition using deeply learned spatially corresponding features. In: 2017 IEEE International Conference on Computer Vision (ICCV), pp. 3829–3838 (2017). https://doi.org/10.1109/ICCV.2017.411
33. Bazrafkan, S., Thavalengal, S., Corcoran, P.: An end to end deep neural network for iris segmentation in unconstrained scenarios. Neural Netw. 106, 79–95 (2018). https://doi.org/10.1016/j.neunet.2018.06.011
34. Nguyen, K., et al.: Iris recognition with off-the-shelf CNN features: A deep learning perspective. IEEE Access 6, 18848–18855 (2018). https://doi.org/10.1109/ACCESS.2017.2784352
35. Liu, G., et al.: An efficient and accurate iris recognition algorithm based on a novel condensed 2-ch deep convolutional neural network. Sensors 21(11), 3721 (2021). https://doi.org/10.3390/s21113721
36. Arsalan, M., et al.: IrisDenseNet: Robust iris segmentation using densely connected fully convolutional networks in the images by visible light and near-infrared light camera sensors. Sensors 18(5), 1501 (2018). https://doi.org/10.3390/s18051501
37. Winston, J.J., et al.: Hybrid deep convolutional neural models for iris image recognition. Multimed. Tools Appl. 81, 9481–9503 (2022). https://doi.org/10.1007/s11042-021-11482-y
38. Sun, J., et al.: Open-set Iris recognition based on deep learning. IET Image Process. 16(9), 2361–2372 (2022). https://doi.org/10.1049/ipr2.12493

How to cite this article: Balashanmugam, T., Sengottaiyan, K., Kulandairaj, M.S., Dang, H.: An effective model for the iris regional characteristics and classification using deep learning alex network. IET Image Process. 17, 227–238 (2023). https://doi.org/10.1049/ipr2.12630